

## PERFORMANCE PREDICTION AND PARAMETRIC OPTIMIZATION OF $\gamma$ -TYPE FREE PISTON STIRLING ENGINE

by

**Xinkui LUO<sup>a</sup>, Xiaojun WANG<sup>a\*</sup>, Chunjie YAN<sup>a</sup>, An ZHANG<sup>a</sup>,  
Xuelin ZHANG<sup>a</sup>, and Wenlian YE<sup>b</sup>**

<sup>a</sup>Key Laboratory of Vacuum Technology and Physics, Lanzhou Institute of Physics,  
Lanzhou, Gansu, China

<sup>b</sup>Key Laboratory of Fluid Machinery and System, Gansu Province,  
College of Power and Energy Engineering, Lanzhou University of Technology,  
Lanzhou, Gansu, China

Original scientific paper  
<https://doi.org/10.2298/TSCI230709232L>

*The free piston Stirling engine is a complex system with multiple parameters strongly coupled. In this study, linear dynamic model and root locus technique are combined to investigate a  $\gamma$ -type free piston Stirling engine. Firstly, brief expressions are derived to predict the operating frequency,  $f$ , phase angle,  $\phi$ , amplitude ratio,  $\eta$ , and output power of  $\gamma$ -type free piston Stirling engine using linear dynamic model. The dynamic parameters are analyzed in detail to reveal their influence on the output performance of the system. Meanwhile, the starting conditions are obtained by root locus technique. Combining the results of the aforementioned two methods, a set of optimized design parameters is identified. The optimum values of  $f$ ,  $\phi$ ,  $\eta$ , and output power are 74.82 Hz, 65.38°, 1.92 W, and 108 W, respectively. Further more, a 60 W  $\gamma$ -type free piston Stirling engine prototype is developed and tested to validate the current model. Compared with the predicted results, the relative errors are less than 4.0% for  $f$ , less than 5.0% for  $\phi$ , less than 2.0% for  $\eta$ , and less than 10.0% for output power. This research provides a reliable approach for the further design of  $\gamma$ -type free piston Stirling engine.*

**Key words:** *free piston Stirling engine, linear dynamic model, root locus technique, performance prediction, parametric optimization*

### Introduction

With the continuous growth of global population and rapid economic development, the energy crisis and environmental protection caused increasingly concerned issues. It has become a common pursuit of researchers all over the world to find alternatives to traditional fossil energy. As a kind of external heated thermal-to-electric conversion device, Stirling engine is characterized by high efficiency, no working medium leakage, self-starting, long service life and silence [1-3]. Stirling engine has broad application prospects in the field of solar power system [4], micro combined heat and power (CHP) technology [5, 6], space thermoelectric conversion devices [7, 8], *etc.*

The free piston Stirling engine (FPSE) was first invented by Beale [9]. Unlike the traditional Stirling engine, FPSE has no mechanical connection between the displacer (dp) and power piston (pp). According to the structural characteristics, FPSE is classified into three

\* Corresponding author, e-mail: 853601824@qq.com

types:  $\alpha$ ,  $\beta$ , and  $\gamma$  [10]. The dp and pp of  $\alpha$ -type FPSE are placed in two separate cylinders to achieve a greater temperature gradient. The dp and pp  $\beta$ -type FPSE are located in the same cylinder to make the engine more compact. The features of  $\gamma$ -type FPSE is that the dp and pp are arranged coaxial but in different cylinders.

Although FPSE has many advantages, it is not an easy task to conduct research because it involves complex physical processes such as thermodynamics, dynamics, mechanics, fluid-structure coupling and so on [11]. In recent years, dynamics and stability criteria attracted the attention of many researchers. Linear dynamic model and root locus technique have been proven to be powerful methods. Chen *et al.* [12] developed a thermodynamic-dynamic coupling model to reveal the phase characteristics of  $\beta$ -type FPSE. Redlich *et al.* [13] derived the locus of the FPSE system determinant root and obtained the criterion of the engine oscillation mode using linear dynamic model. Qiu *et al.* [14] created a linear dynamic simulation model which involves thermodynamic, mechanical, and electro magnetic inputs/outputs for  $\gamma$ -type FPSE. Majidniya *et al.* [15] proposed a combined model of  $\beta$ -type FPSE and permanent magnet linear synchronous motor. Regan *et al.* [16] extended the root locus method to single and dual convertor systems. Riofrio *et al.* [17] presented a control-based design method which view the operation of the system as a feedback system. Standard control tools such as root locus, frequency response (Bode plots), and Nyquist stability criteria were plotted to investigate the dynamic behavior of the system. Zare *et al.* [18] proposed a systematic design method of FPSE based on root locus technique and compared with traditional Beale number method to prove the effectiveness of the new approach. A frequency-based design of FPSE was introduced using genetic algorithm [19]. They studied the effects of the real and imaginary parts of the main closed-loop poles on Stirling engine performance using particle swarm optimization, and concluded that FPSE is more sensitive to changes in the real parts of the main closed-loop poles [20]. A target frequency using genetic algorithm was used to design traveling wave thermoacoustic Stirling engine (TASE) [21]. Then, the energy standpoint and genetic algorithm were utilized to estimate the design parameters of a diaphragm TASE [22]. In addition, a novel analytical and parametrical scheme based on the practical stability and dynamic error to evaluate the stable limit cycle in the dynamical system of FPSE [23]. Ye *et al.* [24] analyzed the main parameters affecting  $\beta$ -type FPSE using linear dynamic model and artificial neural network. They also proposed a non-linear thermodynamic-dynamic coupled model [25, 26]. Kim *et al.* [27] carried out linear dynamic analysis of the operable charge pressure and operating frequency of  $\beta$ -type FPSE. The operating point was predicted using root locus technique.

In this paper, an innovative method for parametric optimization of  $\gamma$ -type FPSE is proposed. Simple expressions are derived to predict operating frequency, phase angle, amplitude ratio and output power of the system. The influence of the dynamic parameters is calculated and analyzed in detail. Then a set of optimized parameters is identified. The current model is verified by experiments on a 60 W  $\gamma$ -type FPSE prototype. This study provides a new approach for the design of  $\gamma$ -type FPSE.

## Mathematical model

### *Liner dynamic model of $\gamma$ -type FPSE*

As illustrated in fig. 1,  $\gamma$ -type FPSE can be divided into three parts: the hot-end, pistons, and linear motor. The hot-end assembly include a heater, a regenerator and a cooler. The pistons assembly is mainly composed of two coaxial pistons. The function of linear motor is to convert mechanical energy into electrical energy. A 60 W  $\gamma$ -type FPSE prototype is depicted in fig. 2.

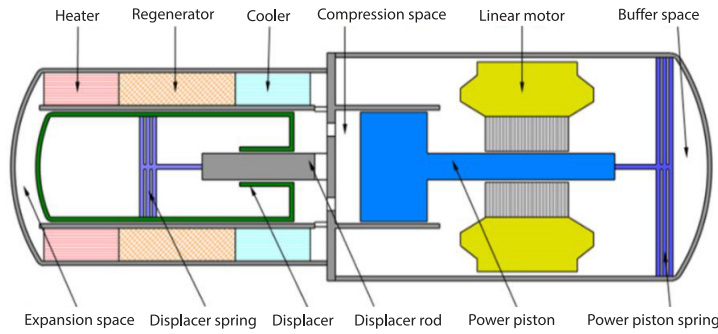


Figure 1. Schematic of  $\gamma$ -type FPSE

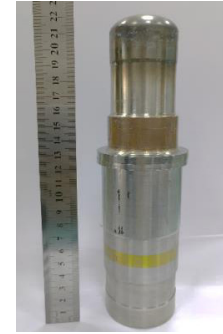


Figure 2. A 60 W  $\gamma$ -type FPSE prototype

Figure 3 shows the force exerted on dp and pp. As mentioned earlier, the feature of  $\gamma$ -type FPSE is that the two pistons are completely independent. Both of dp and pp are dominated by the inertia force, damping force and spring force. The sum of the three forces is the gas force.

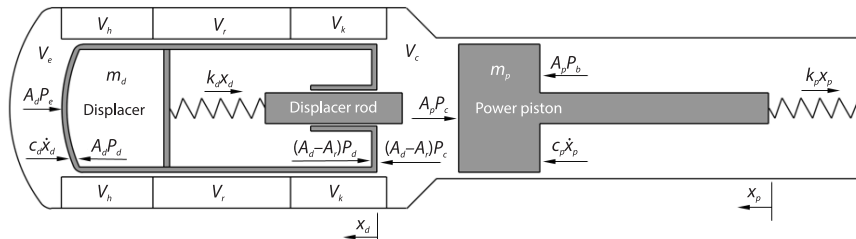


Figure 3. Force diagram of dp and pp

The basic equations of the movement of dp and pp can be written [19, 28]:

$$m_d \ddot{x}_d + C_d \dot{x}_d + K_d x_d = (P_d - P_c) A_d + (P_c - P_d)(A_d - A_r) = -A_r (P - P_0) \quad (1)$$

$$m_p \ddot{x}_p + C_p \dot{x}_p + K_p x_p = -A_p (P_c - P_b) = -A_p (P - P_0) \quad (2)$$

where  $m_d$  and  $m_p$  are the mass of dp and pp,  $x_d$  and  $x_p$  – the displacements of dp and pp,  $C_d$  and  $C_p$  – the damping coefficients of dp and pp,  $K_d$  and  $K_p$  – the spring stiffness of dp and pp,  $A_d$ ,  $A_p$ , and  $A_r$  – the cross-sectional areas of dp, pp, and dp rod, respectively, and  $P_e$ ,  $P_d$ ,  $P_c$ , and  $P_b$  – the gas pressure in the expansion space, dp, compression space and bounce space, respectively,  $P$  and  $P_0$  – the instantaneous and initial charging pressure of the working gas. It can be taken that  $P_e = P_c = P$  when the pressure drop of the working gas-flowing through the heat exchanger (heater, regenerator and cooler) is ignored. The  $P_d = P_b = P_0$  as the pressure fluctuation inside dp and bounce space is negligible.

The FPSE can be regarded as a closed system provided the working medium (generally helium gas) leakage is neglected [28]. According to the classical isothermal analysis model, the pressure of working gas can be expressed from the law of mass conservation and the ideal gas equation of state:

$$P_g = \frac{m_g R_g}{\frac{V_e + V_h}{T_h} + \frac{V_r \ln\left(\frac{T_h}{T_k}\right)}{T_h - T_k} + \frac{V_k + V_c}{T_k}} \quad (3)$$

where  $m_g$  is the total mass of the working gas,  $R_g$  – the gas constant,  $V_h$  and  $V_k$  are the dead volumes of the heater and cooler, respectively,  $V_e$  and  $V_c$  – the instantaneous volumes of the expansion space and compression space, and  $T_e$ ,  $T_h$ ,  $T_k$ , and  $T_c$  – the temperature of the expansion space, heater, cooler and compression space, respectively. In order to simplify the calculation, assuming  $T_e = T_h$  and  $T_c = T_k$ .

For FPSE, the instantaneous pressure can be linearized [16]:

$$P - P_0 = [C_2(A_d - A_r) - C_1 A_d] x_d - C_2 A_p x_p = C_{11} x_d + C_{22} x_p \quad (4)$$

where

$$C_1 = \frac{\partial P_g}{\partial V_e} \bigg|_{V_e = V_{e0}, V_c = V_{c0}} = -m_g R_g \left( \frac{V_e + V_h}{T_h} + \frac{V_r \ln\left(\frac{T_h}{T_k}\right)}{T_h - T_k} + \frac{V_k + V_c}{T_k} \right)^{-2} \frac{1}{T_h}$$

$$C_2 = \frac{\partial P_g}{\partial V_c} \bigg|_{V_e = V_{e0}, V_c = V_{c0}} = -m_g R_g \left( \frac{V_e + V_h}{T_h} + \frac{V_r \ln\left(\frac{T_h}{T_k}\right)}{T_h - T_k} + \frac{V_k + V_c}{T_k} \right)^{-2} \frac{1}{T_k}$$

Substitute eq. (4) into eqs. (1) and (2):

$$\ddot{x}_d = C_{dd} \dot{x}_d + K_{dd} x_d + D_{dp} x_p \quad (5)$$

$$\ddot{x}_p = C_{pp} \dot{x}_p + K_{pp} x_p + D_{pd} x_d \quad (6)$$

where

$$C_{dd} = -\frac{C_d}{m_d}, \quad K_{dd} = \frac{-K_d - A_d C_{11}}{m_d}, \quad D_{dp} = -\frac{A_d C_{22}}{m_d}, \quad C_{pp} = -\frac{C_p}{m_p}$$

$$K_{pp} = \frac{-K_p - A_p C_{22}}{m_p}, \quad D_{pd} = -\frac{A_p C_{11}}{m_p}$$

In FPSE, the displacements of dp and pp are sinusoidal:

$$x_d = X_d \sin(\omega t + \varphi) = X_d \sin(2\pi f t + \varphi) \quad (7)$$

$$x_p = X_p \sin(\omega t) = X_p \sin(2\pi f t) \quad (8)$$

where  $X_d$  and  $X_p$  are the amplitudes of dp and pp,  $\omega$  – the operating angular frequency,  $f$  – the operating frequency, and  $\varphi$  – the phase angle between dp and pp.

The amplitude ratio of dp and pp is defined as eq. (9). In FPSE, larger  $\eta$  indicates that a small dp amplitude can drive a large pp amplitude which is conducive to making the FPSE more compact:

$$\eta = \frac{X_p}{X_d} \quad (9)$$

The formulas of  $f$ ,  $\varphi$ , and  $\eta$  can be derived:

$$f = \frac{1}{2n} \sqrt{\left| \frac{C_{dd} K_{pp} + C_{pp} K_{dd}}{C_{dd} + C_{pp}} \right|} \quad (10)$$

$$\varphi = \arctan\left(\frac{C_{pp}\omega}{\omega^2 + K_{pp}}\right) \quad (11)$$

$$\eta = \frac{|D_{pd}|}{\sqrt{(\omega^2 + K_{pp})^2 + (C_{pp}\omega)^2}} \quad (12)$$

Based on the principle of Stirling cycle [28], the output power of a single cycle can be expressed:

$$W_{CE} = W_C + W_E = \oint PdV_c + \oint PdV_e = \pi X_d X_p \sin \varphi (A_r C_{22} - A_p C_{11}) \quad (13)$$

The total output power (PV) of FPSE:

$$PV = f \times W_{CE} = f \pi X_d X_p \sin \varphi (A_r C_{22} - A_p C_{11}) \quad (14)$$

According to eqs. (1), (2), and (4), the dynamic equations governing the  $\gamma$ -type FPSE system can be described as a state-space form, which resembles the closed-loop feedback control system in modern control theory [19]:

$$\begin{bmatrix} \dot{x}_d \\ \ddot{x}_d \\ \dot{x}_p \\ \ddot{x}_p \end{bmatrix} = \begin{bmatrix} 0 & 1 & 0 & 0 \\ -\frac{K_d}{m_d} & -\frac{C_d}{m_d} & 0 & 0 \\ 0 & 0 & 0 & 1 \\ 0 & 0 & -\frac{K_p}{m_p} & -\frac{C_p}{m_p} \end{bmatrix} \begin{bmatrix} x_d \\ \dot{x}_d \\ x_p \\ \dot{x}_p \end{bmatrix} + \begin{bmatrix} 0 \\ \frac{A_r}{m_d} \\ 0 \\ \frac{A_p}{m_p} \end{bmatrix} \mathbf{u} \quad (15)$$

where  $\mathbf{u}$  is the linear feedback control law.

$$\mathbf{u} = -\mathbf{K}\mathbf{x} = -(p - p_0) = -\begin{bmatrix} C_{11} & 0 & C_{22} & 0 \end{bmatrix} \begin{bmatrix} x_d \\ \dot{x}_d \\ x_p \\ \dot{x}_p \end{bmatrix} \quad (16)$$

where  $\mathbf{K}$  is the state feedback gain matrix [2].

Based on eq. (5) and (6), eq. (15) can be re-written:

$$\begin{bmatrix} \dot{x}_d \\ \ddot{x}_d \\ \dot{x}_p \\ \ddot{x}_p \end{bmatrix} = \begin{bmatrix} 0 & 1 & 0 & 0 \\ K_{dd} & C_{dd} & D_{dp} & 0 \\ 0 & 0 & 0 & 1 \\ D_{pd} & 0 & K_{pp} & C_{pp} \end{bmatrix} \begin{bmatrix} x_d \\ \dot{x}_d \\ x_p \\ \dot{x}_p \end{bmatrix} \quad (17)$$

Through the previous analysis, a complete dynamic model of  $\gamma$ -type FPSE is established. Equations (10)-(14) provide reliable analytic expressions to predict the significant output parameters of the system. Equations (15)-(17) illustrates another powerful approach to obtain the starting conditions and stability criterion of the system.

### Model validation

In order to verify the accuracy of the aforementioned mathematical model, the parameters at the stable working point of a 60 W  $\gamma$ -type FPSE (named LIP-60) developed by ourselves

are calculated. The results predicted by the current model are compared with the experimental results. Table 1 presents the basic parameters of the LIP-60 FPSE. The experimental system is shown in fig. 4.

**Table 1. The basic parameters of the LIP-60 FPSE**

Parameters	Symbol	Values	Unit
Charge pressure	$P_0$	$3.0 \cdot 10^6$	[Pa]
Cross-section area of pp	$A_p$	$4.337 \cdot 10^{-4}$	[m <sup>2</sup> ]
Cross-section area of dp	$A_d$	$9.079 \cdot 10^{-4}$	[m <sup>2</sup> ]
Crosscut area of dp rod	$A_r$	$5.027 \cdot 10^{-5}$	[m <sup>2</sup> ]
Volume of expansion space	$V_{eo}$	$3.15 \cdot 10^{-6}$	[m <sup>3</sup> ]
Volume of compression space	$V_{co}$	$6.30 \cdot 10^{-6}$	[m <sup>3</sup> ]
Porosity of the regenerator	$\varepsilon$	0.9	[-]

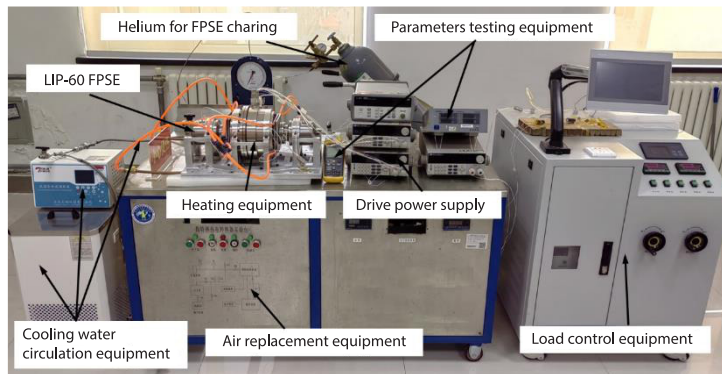


**Figure 4. The LIP-60 FPSE experimental system**

As listed in tab. 2, when the prototype works at stable working conditions, the results predicted by the current model are in good agreement with the experimental results. The relative errors are mainly caused by non-linear factors (pressure drop, temperature inhomogeneity, shuttle loss, *etc.*). Actually, the current model can accurately predict the performance and stability of the  $\gamma$ -type FPSE when the parameters change.

**Table 2. Comparison of current model predictions with experimental results of LIP-60 FPSE**

	$f$ [Hz]	$\varphi$ [°]	$\eta$ [-]	PV [W]
Current model	74.82	65.38	1.92	108
Experimental results	73.3	62.85	1.97	99.93
relative error	2.07%	4.03%	2.54%	8.08%

\* the relative error is defined as: current model prediction – experimental result/experimental result.

## Results and discussion

Equations (10)-(14) provide reliable method to predict  $f$ ,  $\varphi$ ,  $\eta$ , and PV, which are chosen as optimization objectives. Obviously, multiple parameters will affect the predicted results.

Equations (15)-(17) present that the stability of  $\gamma$ -type FPSE can be investigated by means of modern control theory. It is noted that the system should be unstable or at least marginally stable in the linear dynamic sense, which is the basic criterion for FPSE system to operate properly. Seen from eq. (17), the state matrix of  $\gamma$ -type FPSE system is fourth order. Therefore, it has four eigenvalues, in which only a pair of conjugate roots whose real part is greater than zero is the dominant pole. The imaginary part of the dominant pole is equal to the operating frequency of the FPSE [2].

### Influence analysis of dynamic parameters

#### Mass of dp and pp ( $m_d$ and $m_p$ )

Figures 5(a) and 5(b) present that with the increase of  $m_d$  and  $m_p$ ,  $f$  decreases, while  $\eta$  increases initially and then decreases. Figures 5(c) and 5(d) show that with the increase of

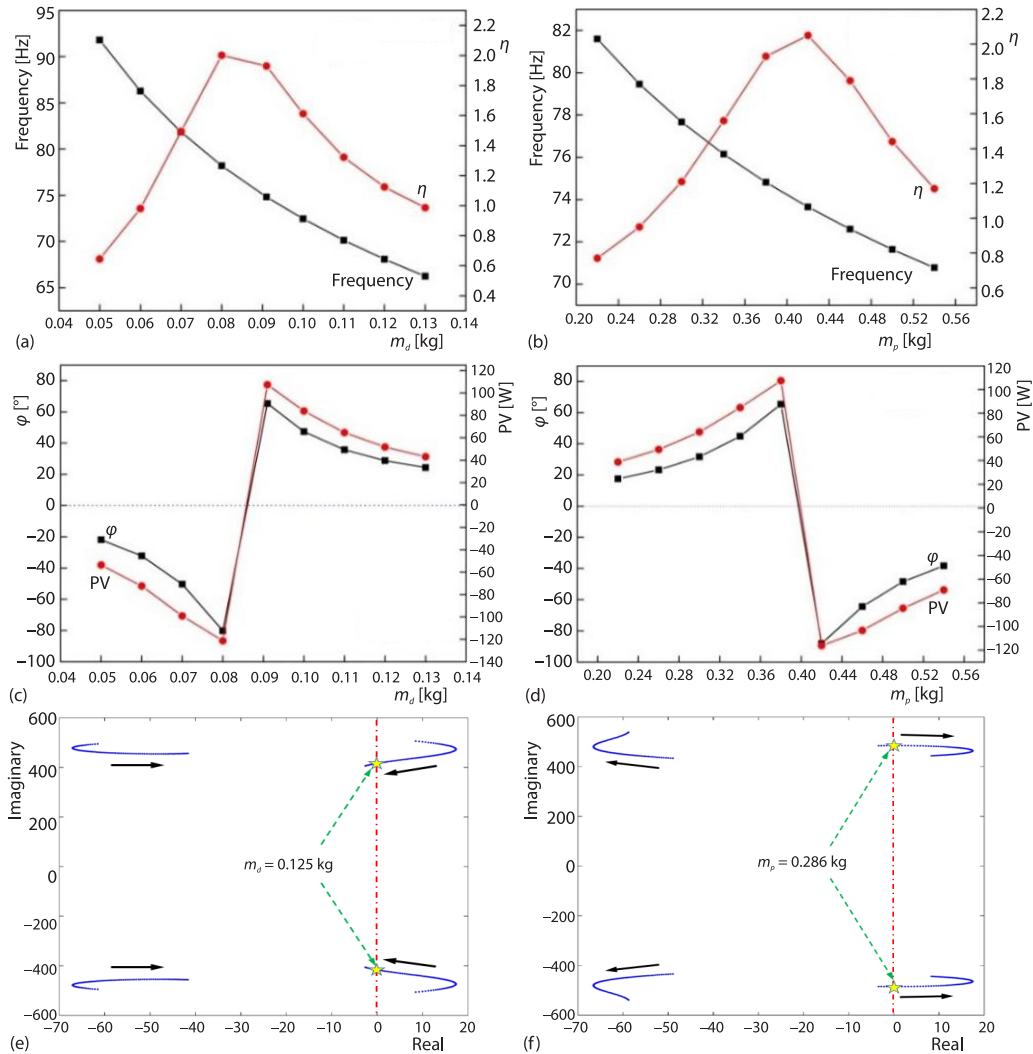


**Figure 5.** Influence of  $m_d$  and  $m_p$ ; (a)  $f$  and  $\eta$  ( $m_d$ ), (b)  $f$  and  $\eta$  ( $m_p$ ), (c)  $\phi$  and PV ( $m_d$ ), (d)  $\phi$  and PV ( $m_p$ ), (e) root locus when  $0.05 \text{ kg} < m_d < 0.13 \text{ kg}$ , and (f) root locus when  $0.023 \text{ kg} < m_p < 0.54 \text{ kg}$

$m_d$  and  $m_p$ ,  $\varphi$ , and PV has the same trend. That is, when  $m_d$  is greater than a critical value ( $m_d = 0.083$  kg) and  $m_p$  is less than a critical value ( $m_p = 0.418$  kg),  $\gamma$ -type FPSE can be started. Meanwhile,  $\varphi$  and PV decrease with the increase of  $m_d$ , while increase with the increase of  $m_p$ . Figure 5(e) presents that with the increase of  $m_d$ , the real part of the eigenvalue of the state matrix moves from the right side to the left side of zero point, resulting in that FPSE cannot operate. The maximum value of  $m_d$  is 0.125 kg. Thus, the range of  $m_d$  can be determined as  $0.083$  kg  $< m_d < 0.125$  kg. Similarly, the range of  $m_p$  can be obtained as  $0.286$  kg  $< m_p < 0.418$  kg.

#### Stiffness of dp and pp ( $K_d$ and $K_p$ )

As seen in figs. 6(a) and 6(b),  $f$  increases as  $K_d$  and  $K_p$  increase. While  $\eta$  increases initially and then decreases with the increase  $K_d$  of  $K_p$ . Figures 6(c) and 6(d) indicate that  $\varphi$  and PV have an opposite trend with the increase of  $K_d$  and  $K_p$  compared with the influence of  $m_d$  and  $m_p$ . In other words, when  $K_d$  is less than the critical value ( $K_d = 24420$  N/m) and  $K_p$  is larger than the critical value ( $K_p = 60000$  N/m), FPSE can be started. Additionally,  $K_d$  and  $K_p$  are limited to a narrow range around the critical values in an effort to enable  $f$ ,  $\varphi$ ,  $\eta$ , and PV within an suitable range. When  $K_p$  is larger than 75000 N/m, PV  $< 90$  W, which indicates that the out performance of the system declines. Figures 6(e) and 6(f) present the influence of spring stiffness on the stability of the system. When  $K_d$  and  $K_p$  increases, the real part of the eigenvalue of the state matrix moves from the left side to right the side of zero point, indicating in that FPSE can be started. The lower limit value of  $K_d$  is 16800 N/m. Thus the range of  $K_d$  is limited to  $16800$  N/m  $< K_d < 24400$  N/m. The lower limit value of  $K_p$  is 38170 N/m. In conjunction with Figures 6(a)-6(d), the range of  $K_p$  that enable FPSE to be started and work efficiently is  $60000$  N/m  $< K_p < 75000$  N/m.

#### Damping ratio of dp and pp ( $\zeta_d$ and $\zeta_p$ )

As a two-degree-of-freedom vibration system [27], the damping sources of dp and pp of FPSE are mainly mechanical damping, gas damping, electromagnetic damping, etc. In general, dp and pp are under damped ( $\zeta_d < 1$  and  $\zeta_p < 1$ ) in FPSE. The less damping, the lower the loss of the system will be. However, the dp and pp assemblies involve several clearance seals. The proportion of gas leakage in the clearance and mechanical loss needs to be balanced. Figures 7(a) and 7(b) present that  $f$  increases slowly with the increase of  $\zeta_d$ , and decreases slowly with the increase of  $\zeta_p$ . The  $\eta$  increases slowly with the increase of  $\zeta_d$ , while decreases rapidly with the increase of  $\zeta_p$ . As depicted in figs. 7(c) and 7(d), with the increase of  $\zeta_d$  and  $\zeta_p$ ,  $\varphi$ , and PV increase. Although  $\zeta_d$  and  $\zeta_p$  predicted by current model seem to be beneficial to the output parameters. But the loss caused by damping will significantly reduce the efficiency of FPSE system. Furthermore, in order to obtain reasonable  $\eta$  and  $\varphi$ ,  $\zeta_d$ , and  $\zeta_p$  need to be as small as possible. Figures 7(e) and 7(f) indicate that when  $\zeta_d$  and  $\zeta_p$  increase, the real part of the eigenvalue of the state matrix moves from the right side to left the side of zero point.

The critical value of  $\zeta_d$  and  $\zeta_p$  are 0.097 and 0.12, respectively. That is, when  $\zeta_d < 0.097$  and  $< 0.12$ , FPSE can be started. When  $\zeta_d$  and  $\zeta_p$  are greater than the critical value, the FPSE system will fail to be started due to the inability to overcome the damping effect. It should be noted that the upper limits of  $\zeta_d$  and  $\zeta_p$  obtained by root locus method refer to the maximum damping ratio to enable the initiation of the FPSE system. In fact,  $\zeta_d$  and  $\zeta_p$  should be strictly controlled to increase the output power of the system. Based on the predicted results, the reasonable range of  $\zeta_d$  and  $\zeta_p$  are:  $0.028 < \zeta_d < 0.097$  and  $0.06 < \zeta_p < 0.12$ .

According to the aforementioned analysis, for the 60 W  $\gamma$ -type FPSE prototype, a set of optimized parameters to match the operating parameters and maximize the output power is given in tab. 3.

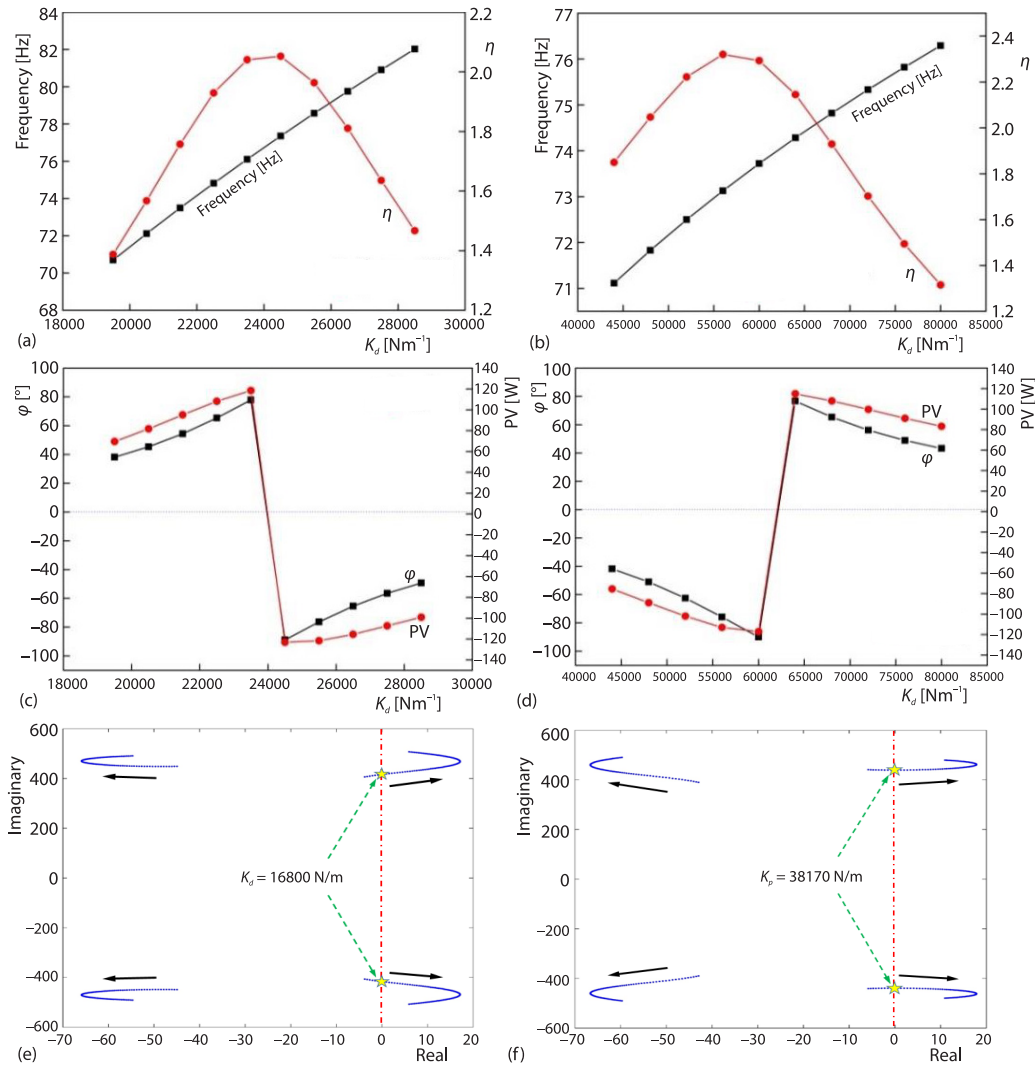


**Figure 6. Influence of  $K_d$  and  $K_p$ ; (a)  $f$  and  $\eta$  ( $K_d$ ), (b)  $f$  and  $\eta$  ( $K_p$ ), (c)  $\varphi$  and PV ( $K_d$ ), (d)  $\varphi$  and PV ( $K_p$ ), (e) locus when  $16000 \text{ N/m} < K_d < 30000 \text{ N/m}$ , and (f) root locus when  $33000 \text{ N/m} < K_p < 80000 \text{ N/m}$**

### Experimental results and analysis

Figure 8 presents the trend of  $f$  with the increase of the heating temperature,  $T_h$ . The  $f$  predicted by the dynamic model is higher than the experimental results. The maximum relative error is less than 4.0%, which indicates that the current model can accurately predict the operating frequency of  $\gamma$ -type FPSE. The results show that  $f$  increases gradually with the increase of  $T_h$ . It is mainly because the pressure of the working gas in the FPSE rises with the increase of  $T_h$ . Furthermore, the stiffness of the gas spring of dp increases, leading to  $f$  increases.

As interpreted in fig. 9,  $\varphi$  decreases with the increase of  $T_h$ . The predicted results of the current model and the experimental results have the same trend. The relative error is within 5%. In fact,  $\varphi$  is maintained when FPSE works at a constant heating temperature, which is a

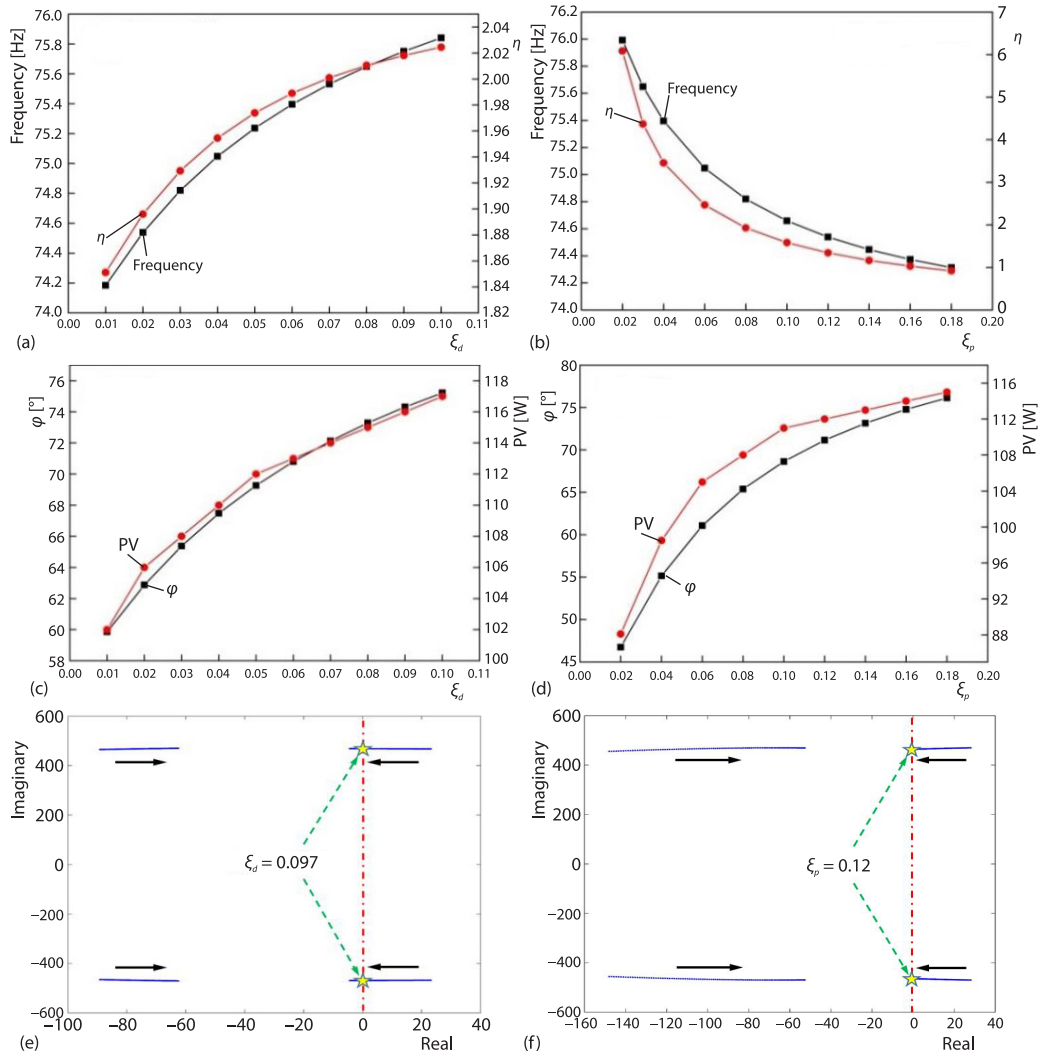


**Figure 7. Influence of  $\xi_d$  and  $\xi_p$  on FPSE; (a)  $f$  and  $\eta$  ( $\xi_d$ ), (b)  $f$  and  $\eta$  ( $\xi_p$ ), (c)  $\varphi$  and PV ( $\xi_d$ ), (d)  $\varphi$  and PV ( $\xi_p$ ), (e) root locus when  $0.01 < \xi_d < 0.1$ , and (f) root locus when  $0.02 < \xi_p < 0.15$**

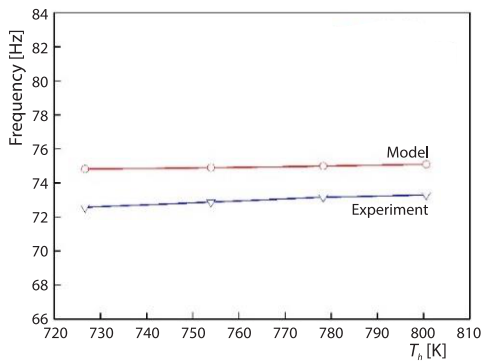
prerequisite for FPSE to work stably. According to the current model and experimental results,  $\gamma$ -type FPSE can work stably and efficiently when the phase angle is in the range of  $60^\circ \sim 70^\circ$ .

Figure 10 displays that  $\eta$  increases with the increase of  $T_h$ . According to eqs. (1) and (2), the gas force exerted on dp and pp is proportional to  $(p-p_0)A_r$  and  $(p-p_0)A_p$ , respectively. As mentioned earlier,  $p$  increases as  $T_h$  increases. Owing to  $A_r < A_p$ , the gas force exerted on pp is greater than that exerted on dp. Therefore, when  $T_h$  increases, the amplitude growth of pp is faster than that of dp, so  $\eta$  goes up. The relative error between the model and the experimental results is within 2%.

As depicted in fig. 11, PV increases as  $T_h$  increases. The maximum relative error between the model and experimental results is close to 10%. Owing to the flow resistance of the heat exchanger and the loss of the regenerator are not considered, the results predicted by

**Table 3. A set of optimized design parameters of the 60 W  $\gamma$ -type FPSE prototype**

Parameters	Symbols	Values	Units
Charge pressure	$p_0$	$3.0 \cdot 10^6$	[Pa]
Heater temperature	$T_h$	800	[K]
Cooler temperature	$T_k$	300	[K]
Mass of dp	$m_d$	0.091	[kg]
Mass of pp	$m_p$	0.38	[kg]
Spring stiffness of dp	$K_d$	21500	[Nm <sup>-1</sup> ]
Spring stiffness of pp	$K_p$	68000	[Nm <sup>-1</sup> ]
Damping ratio of dp	$\zeta_d$	0.03	[-]
Damping ratio of pp	$\zeta_p$	0.08	[-]
Operating frequency	$f$	74.82	[Hz]
Phase angle of dp and pp	$\varphi$	65.38	[°]
Amplitude ratio of dp and pp	$\eta$	1.92	[-]
Output power	PV	108	[W]



**Figure 8. Trend of  $f$  with  $T_h$**

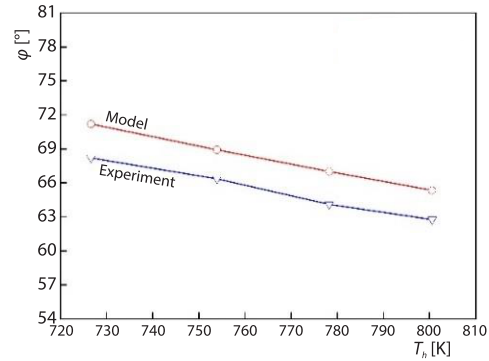


**Figure 9. Trend of  $\varphi$  with  $T_h$**

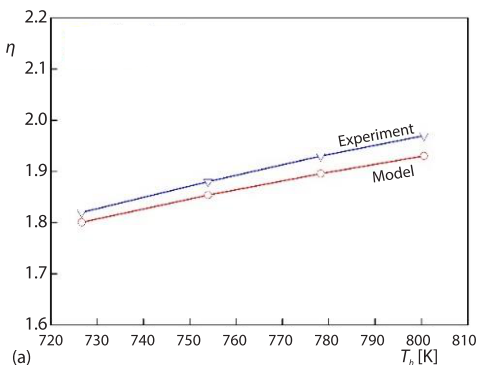


**Figure 10. Trend of  $\eta$  with  $T_h$**

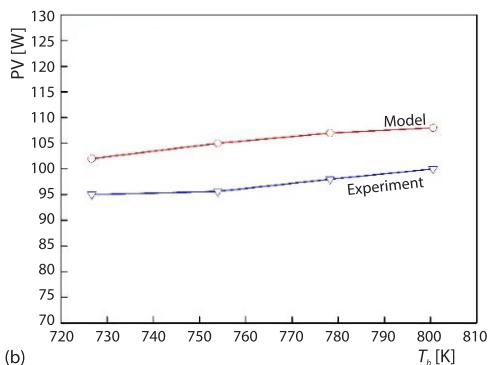


**Figure 11. Trend of PV with  $T_h$**

current model are always greater than that of the experiment. Further, the output electric power is measured. When the heating temperature reaches 800 K, the output electric power is 64.6 W at an operating frequency of 73.3 Hz.

## Conclusions

In this study, linear dynamic model combined with root locus technique are applied to predict the output performance and optimize parameters of  $\gamma$ -type FPSE. Reliable expressions of the operating frequency, phase angle, amplitude ratio and output power are derived. The influence of the key dynamic parameters on the output performance of the system is analyzed in detail. The start-up characteristics of the system are discussed. The results predicted by the current model are compared with the experimental results. The conclusions are as follows.

- A total of six dynamic parameters, including the mass of dp and pp, stiffness of dp and pp, and damping coefficient of dp and pp are selected as variables. The operating frequency, phase angle, piston's amplitude ratio and PV power are chosen as optimization objective. Each variable is studied in detail with the aim of maximizing PV power.
- An innovative method for optimizing dynamic parameters of  $\gamma$ -type FPSE is proposed. The lower limits of  $m_d$ ,  $K_p$ ,  $\zeta_d$ , and  $\zeta_p$ , as well as the upper limits of  $m_p$  and  $K_d$  can be predicted by the linear dynamic model. While the upper limits of  $m_d$ ,  $K_p$ ,  $\zeta_d$ , and  $\zeta_p$ , as well as the lower limits of  $m_p$  and  $K_d$  can be obtained by root locus technique. The range of each dynamic parameter has been determined by combining the results of these two methods.
- A set of optimized design parameters of 60 W  $\gamma$ -type FPSE is identified. The optimum values of  $f$ ,  $\varphi$ ,  $\eta$ , and PV are 74.82 Hz, 65.38°, 1.92 and 108 W, respectively.
- A 60 W  $\gamma$ -type FPSE prototype was developed and tested. The results show that the relative errors between current model predictions and experimental results are less than 4.0% for  $f$ , less than 5.0% for  $\varphi$ , less than 2.0% for  $\eta$ , and less than 10.0% for PV. When the heating temperature is 800 K, the output power is 64.6 W at an operating frequency of 73.3 Hz.

## Acknowledgment

This work is financially supported by the National Natural Science Foundation of China (No. 52106027) and Key Laboratory of Vacuum Technology and Physics Foundation of China (No. 6142207210201).

## Nomenclature

$A$  – cross-sectional area, [m<sup>2</sup>]  
 $C_d$  – damping coefficient of displacer, [Nsm<sup>-1</sup>]  
 $C_p$  – damping coefficient of power piston, [Nsm<sup>-1</sup>]  
 $D$  – ratio of damping coefficient to the mass of the piston, [s<sup>-1</sup>]  
 $f$  – operating frequency, [Hz]  
 $K_d$  – spring stiffness of displacer, [Nm<sup>-1</sup>]  
 $K_p$  – spring stiffness of power piston, [Nm<sup>-1</sup>]  
 $m$  – mass, [kg]  
 $p$  – instantaneous pressure, [Pa]  
 $p_0$  – charge pressure, [Pa]  
 $T$  – temperature, [K]  
 $t$  – time, [s]  
 $V$  – volume, [m<sup>3</sup>]  
 $W$  – output power, [W]  
 $x$  – displacement, [m]  
 $\dot{x}$  – speed, [ms<sup>-1</sup>]  
 $\ddot{x}$  – acceleration, [ms<sup>-2</sup>]

### Greek symbols

$\varepsilon$  – porosity of the regenerator

$\eta$  – amplitude ratio of displacer and power piston  
 $\xi$  – damping ratio  
 $\varphi$  – phase angle of displacer and power piston, [°]  
 $\omega$  – angular frequency, rad/s

### Subscripts

b – bounce space  
c – compression space  
co – compression space at a static equilibrium state  
d – displacer  
e – expansion space  
eo – expansion space at a static equilibrium state  
g – gas  
h – heater  
k – cooler  
p – power piston  
r – regenerator

### Acronyms

dp – displacer  
pp – power piston

## References

- [1] Walker, G., *et al.*, *Free Piston Stirling Engines*, Springer., Berlin, Germany, 1985
- [2] Zare, S. H., *et al.*, Free Piston Stirling Engines: A Review, *International Journal of Energy Research*, 44 (2020), 7, pp. 1-32
- [3] Zare, S. H., *et al.*, Thermoacoustic Stirling engines: A Review, *International Journal of Green Energy*, 20 (2023), 1, pp. 89-111
- [4] Qiu, S. G., *et al.*, Development of an Integrated Thermal Energy Storage and Free-Piston Stirling Generator for a Concentrating Solar Power System, *Energies*, 10 (2017), 9, pp.1-17
- [5] Zhu, S. M., *et al.*, A Review of Stirling-Engine-Based Combined Heat and Power Technology, *Applied Energy*, 294 (2021), 116965
- [6] Qiu, S. G., *et al.*, Development of an Advanced Free-Piston Stirling Engine for Micro Combined Heating and Power Application, *Applied Energy*, 235 (2019), Feb., pp. 987-1000
- [7] Wilson, S., Overview of Stirling Technology Research at NASA Glenn Research Center, *Proceedings*, 13<sup>th</sup> International Energy Conversion Engineering Conference, Hampton, Va., USA, 2015
- [8] De, M., *et al.*, Thermodynamic-Dynamic Coupling of a Stirling Engine for Space Exploration, *Thermal Science and Engineering Progress*, 32 (2022), 101320
- [9] Beale, W., *Free-Piston Stirling Engines-Some Model Tests and Simulations*, SAE Technical Paper, 1969-02-01, 1969
- [10] Urieli, I., *et al.*, *Stirling Cycle Engine Analysis*, Adam Hilger Ltd., Bristol, N. Y., USA, 1984
- [11] Majidniya, M., *et al.*, Performance Simulation by a Non-Linear Thermodynamic Model for a Free Piston Stirling Engine with a Linear Generator, *Applied Thermal Engineering*, 184 (2020), 116128
- [12] Chen, P. F., *et al.*, Parametric Investigation of the Phase Characteristics of a Beta-Type Free Piston Stirling Engine Based on a Thermodynamic-Dynamic Coupled Model, *Energy*, 219 (2021), 119658
- [13] Redlich, R. W., *et al.*, Linear Dynamics of Free-Piston Stirling Engines, *Proc. Inst. Mech. Eng., Part A, Power Process Eng.*, 199 (1985), Aug., pp. 203-213
- [14] Qiu, S. G., *et al.*, Linear Dynamic Modelling and Numerical Simulation of an STC Stirling Converter, *Proceedings*, 1<sup>th</sup> International Energy Conversion Engineering Conference, Portsmouth, Va., USA, 2003
- [15] Majidniya, M., *et al.*, Non-Linear Modelling of a Free Piston Stirling Engine Combined with a Permanent Magnet Linear Synchronous Machine, *Applied Thermal Engineering*, 184 (2019), 114544
- [16] Regan, T. F., *et al.*, Stirling System Modelling for Linear Dynamics Analysis, *Proceedings*, 3<sup>th</sup> International Energy Conversion Engineering Conference, San Francisco, Cal., USA, 2005
- [17] Riofrio, J. A., *et al.*, Control Based Design of Free Piston Stirling Engine, *Proceedings*, American Control Conference, Seattle, Wash., USA, 2008, pp. 1533-1538
- [18] Zare, S. H., *et al.*, From Beale Number to Pole Placement Design of a Free Piston Stirling Engine, *Arch Mech Eng.*, 64 (2017), 4, pp. 499-518
- [19] Zare, S. H., *et al.*, Frequency-Based Design of a Free Piston Stirling Engine Using Genetic Algorithm, *Energy*, 109 (2016), Aug., pp. 466-480
- [20] Zare, S. H., *et al.*, Applying Particle Swarm Optimization Study the Effect of Dominant Poles Places on Performance of a Free Piston Stirling Engine, *Arab. J. Sci. Eng.*, 44 (2019), Dec., pp. 5657-5669
- [21] Zare, S. H., *et al.*, Design of a Traveling Wave Thermo-Acoustic Engine Based on Genetic Algorithm, *Int. J. Energy Res.*, 43 (2019), 14, pp. 1-12
- [22] Zare, S. H., *et al.*, Assessment of a Diaphragm Thermoacoustic Stirling Engine Using the Energy Standpoint and Genetic Algorithm., *Int. J. Energy Environ. Eng.*, 14 (2022), Oct., pp. 743-755
- [23] Zare, S. H., *et al.*, Analytical Investigation of Free Piston Stirling Engines Using Practical Stability Method., *Chaos, Solitons and Fractals*, 167 (2023), 113082
- [24] Ye, W. L., *et al.*, Application of Artificial Neural Network for Predicting the Dynamic Performance of a Free Piston Stirling Engine, *Energy*, 194 (2020), 116912
- [25] Ye, W. L., *et al.*, Parametric Study of Gamma-Type Free Piston Stirling Engine Using Non-Linear Thermodynamic-Dynamic Coupled Model, *Energy*, 211 (2020), 18458
- [26] Ye, W. L., *et al.*, Exergy Loss Analysis of the Regenerator in a Solar Stirling Engine, *Thermal Science*, 22 (2018), Suppl. 2, pp. S729-S737
- [27] Kim, D. J., *et al.*, Linear Dynamic Analysis of Free-Piston Stirling Engines on Operable Charge Pressure and Working Frequency along with Experimental Verifications, *Appl. Sci.*, 11 (2021), 5205
- [28] Walker, G., *Stirling Engines*, Oxford University Press, UK, 1980

Paper submitted: July 9, 2023

Paper revised: September 17, 2023

Paper accepted: September 21, 2023

© 2024 Society of Thermal Engineers of Serbia

Published by the Vinča Institute of Nuclear Sciences, Belgrade, Serbia.

This is an open access article distributed under the CC BY-NC-ND 4.0 terms and conditions